Numerical study of HCl and SO2 impact on potassium emissions in pulverized-biomass combustion

Kaidi Wan, Zhihua Wan, Jun Xia, Luc Vervisch, Pascale Domingo, Yu Lv, Yingzu Liu, Yong He, Kefa Cen

Numerical study of HCl and SO₂ impact on potassium emissions in pulverized-biomass combustion

Kaidi Wan[1], Zhihua Wang[2,*], Jun Xia[3,*], Luc Vervisch[1], Pascale Domingo[1], Yu Lv[4], Yingzu Liu[2], Yong He[2], Kefa Cen[2]

1. CORIA – CNRS, Normandie Université,
INSA de Rouen, 76800 Saint-Etienne-du-Rouvray, France

2. State Key Laboratory of Clean Energy Utilization,
Zhejiang University, Hangzhou 310027, China

3. Department of Mechanical and Aerospace Engineering & Institute of Energy Futures,
Brunel University London, Uxbridge UB8 3PH, UK

4. Department of Aerospace Engineering, Mississippi State University,
Mississippi State, MS 39762, USA

* Corresponding authors: wangzh@zju.edu.cn (Zhihua Wang); jun.xia@brunel.ac.uk (Jun Xia).

Abstract

The potassium vapor released during the combustion of biomass are known to result in serious ash deposition, fouling and corrosion issues of biomass furnaces. To develop potassium control technologies to mitigate these issues and achieve clean utilization of biomass fuel, a better understanding of the fundamental formation and transformation mechanisms of potassium in biomass combustion is essentially required. In the present study, potassium emissions during pulverized-biomass combustion, for the first time, have been simulated in both one-dimensional (1D) premixed/diffusion flames of the biomass volatile and an early-stage two-dimensional (2D) pulverized-biomass flame. The properties of corn straw are used. The volatile-gas combustion is described by the DRM22 skeletal mechanism, while the homogeneous reaction of potassium species is modeled using a detailed mechanism encompassing the elements K, C, H, O, Cl and S. The initial species of K, Cl and S in the volatile gas is set to be KOH, HCl and SO₂, respectively. The transformation characteristics of the potassium species are numerically investigated in both the 1D and 2D flames. Results show that KOH is the most significant potassium product under fuel-lean,

28   stoichiometric and fuel-rich conditions, while the productions of sulfurous and chloric potassium

29   species are secondary. Parametric studies with HCl, SO_2 or both species replaced with N_2 in volatile

30   gas are then performed to study their impacts on potassium emission characteristics in both the 1D

31   and 2D flames. The results indicate that HCl has a stronger ability to react with potassium species

32   than SO_2.

34

35   **1. Introduction**

36   As a renewable fuel source, biomass resources have been utilized to supply 10–15% of the

37   worldwide energy consumption [1], especially with an increasing application in the production of

38   thermal power. However, advanced biomass utilization is significantly limited by severe ash

39   formation and deposition problems resulting from alkali metal issues [2]. Potassium (K) is usually

40   rich in biomass, since it is an important element for plants. The potassium vapor released during the

41   combustion of biomass is easy to condense on heat transfer surfaces and form an initial sticky layer,

42   which then captures fly ash and therefore results in rapid ash deposition [3, 4]. In addition, potassium

43   also reacts with chlorine and sulfur species to form complex compound, which leads to serious

44   fouling and corrosion issues [5, 6]. Thus, understanding the fundamental formation and

45   transformation mechanisms of potassium in biomass combustion is essential for the development of

46   potassium control technologies and a better utilization of this renewable fuel [7-9].

47   Experimental research on the release and reacting dynamics of potassium evolves from offline

48   sampling techniques to online measurement methods using laser diagnostics [2, 10-12].

49   Non-intrusive, time-resolved laser techniques, e.g., tunable diode laser absorption spectroscopy

50 (TDLAS) [13], collinear photo-fragmentation atomic absorption spectroscopy (CPFAAS) [14] and

51 laser induced fragmentation fluorescence (ELIF) [15], can directly capture the dynamic release

52 process of potassium during biomass combustion. In our recent study [16], the release of atomic and

53 elemental potassium from a burning biomass pellet has been quantitatively measured via planar

54 laser-induced fluorescence (PLIF) and multi-point laser-induced breakdown spectroscopy (LIBS)

55 methods.

56   On the modeling side, Zhang et al. [17] proposed an one-step Arrhenius potassium release

57 model during the combustion of a pinewood pellet. In our recent work [16], a two-step model was

58 developed to describe the potassium release during both the pyrolysis and char burnout stages of two

59 biomass samples, based on simultaneous measurements of the pellet-surface temperature, pellet

60 diameter and potassium release of a burning biomass pellet. Since the pellet diameter and burnout

61 time of biomass in these studies are on the same order of magnitude as in a typical circulating

62 fluidized bed (CFB) boiler, these potassium release models are suitable for CFB combustion [18].

63 Potassium release models for pulverized-biomass combustion are still required to be developed.

64   Considering the post-release homogeneous reactions of alkali species, it has been found that the

65 main alkali species are atomic K/Na, KOH/NaOH and KCl/NaCl in chemical equilibrium of

66 post-combustion gases [19], which can be well predicted by thermodynamic equilibrium calculation,

67 e.g., [18-20]. A detailed chemical reaction mechanism for alkali species has been proposed by

68 Glarborg and Marshall [21], and validated with experimental data on sulfation of potassium chlorides.

69 However, the numerical investigation on reaction dynamics of alkali species in turbulent reacting

70 flows is still quite limited. Most of the relevant research employs Reynolds-averaged Navier-Stokes

71 (RANS) simulation (e.g. [22, 23]) with simplified alkali reaction mechanisms to study the response

72   of potassium in biomass combustion.

73   With the rapid increase of computing capacity in recent years, computational fluid dynamics

74   (CFD) approaches for multi-phase flows are evolving towards high-fidelity methods, i.e., direct

75   numerical simulation (DNS, e.g., [24-26]) and large-eddy simulation (LES, e.g. [27-34]). The two

76   high-fidelity methods have shown advantages over RANS on the prediction of local gas temperature

77   and species distributions. Our previous work [26, 34] on pulverized-coal combustion demonstrated

78   that DNS and LES can provide detailed physical insights into complex multi-phase reacting flow

79   dynamics and the homogeneous evolution of alkali species.

80   In sum, the reaction dynamics of potassium species in pulverized-biomass combustion have not

81   been fully revealed by previous studies. In the present work, the responses of potassium species to

82   one-dimensional (1D) premixed/diffusion flames of biomass volatile are firstly investigated. Then,

83   the transformation dynamics of potassium species in a two-dimensional (2D) early-stage

84   pulverized-biomass flame are numerically studied, excluding char combustion. Information about the

85   major potassium product under various conditions and the comparison between the impacts of HCl

86   and SO_2 on potassium conversion are revealed, which could potentially benefit the biomass

87   combustion community. The full detailed potassium mechanism including the elements K, C, H, O, S

88   and Cl proposed by Glarborg and Marshall [21] is utilized to model the potassium reactions during

89   the simulation. It should be noted that Glarborg and Marshall [21] have carefully validated their

90   detailed potassium mechanism against the experimental results of the homogeneous sulfation of

91   potassium chloride at combustion conditions. The readers might notice that there exists a newer

92   version of potassium mechanism by Hindiyarti et al. [35], which includes additional sulfation

93   pathways of potassium to mainly improve the prediction of the mechanism at lower temperatures

2. One-dimensional premixed/diffusion flames of biomass volatile

The reaction dynamics of potassium species in 1D premixed/diffusion flames of biomass volatile are studied. The volatile is released from corn straw [16], for which the chemical analysis data is shown in Table 1. The combustion of biomass volatile is modeled by the previously validated DRM22 skeletal mechanism involving 22 chemical species and 104 elementary reactions, which is proposed by Kazakov and Frenklach [37]. The bio-chemical percolation devolatilization (bio-CPD) model [38-40] is used to preliminary obtain the compositions of the volatile fuels and in which the Tar species is replaced by C_2H_2 [32]. Then the obtained compositions are adjusted to fulfill the elemental mass conservation and the lower heating value of the corn straw, as in [30, 33, 34]. The final volatile compositions used in the present study is shown in Table 2.

Table 1. Chemical analyses of corn straw.

Proximate analysis (wt%)				Ultimate analysis (wt%)				
M_{ad}	A_{ad}	V_{ad}	FC_{ad}	C_{daf}	H_{daf}	N_{daf}	S_{daf}	O_{daf}
11.6	7.9	64.2	16.3	43.9	4.5	1.8	0.4	49.3
Ash analysis (wt%)							Cl_{ad}	K_{ad}
SiO_2	Al_2O_3	Fe_2O_3	CaO	MgO	K_2O	Na_2O	(mg/g)	(mg/g)
47.52	5.64	1.04	4.51	12.6	7.87	1.97	1.34	13.1

110

Table 2. Modeled volatile-gas compositions of corn straw.

Hydrocarbon volatile compositions (mass fractions)					
CH_4	C_2H_2	CO	H_2	CO_2	H_2O
0.0322	0.1805	0.2536	0.0215	0.1853	0.3024
Non-hydrocarbon volatile compositions (mass fractions)					
KOH	HCl	SO_2			
0.0147	0.0018	0.0080			

112

Similar as previous studies on sodium emissions in coal combustion [41], KOH is set as the

initial species of K, while HCl and SO_2 are set as the initial species of Cl and S, respectively.

According to our previous experimental data [16], the percentage of potassium which is releasable

during the biomass pyrolysis stage is set to 58.1%. Since the release of chlorine and sulfur has not

been measured, their releasable proportions during the pyrolysis are both set to 87.3%, the volatile

yields ratio predicted by the bio-CPD model [38], based on the consideration chlorine and sulfur can

be fully released during the pyrolysis and char stages of biomass combustion. Mass fractions of

KOH, HCl and SO_2 in the volatile can then be obtained, as shown in Table 2. The detailed alkali

mechanism developed by Glarborg and Marshall [21] includes elementary reactions over Na, K, C,

H, O, S and Cl. Here, the element Na is not considered, which leads to a detailed mechanism of

potassium involving 35 species and 153 elementary reactions.

To study the potassium reactions under the premixed condition, a 1D freely propagating

premixed flame of the biomass volatile is simulated using CANTERA [42]. The inlet volatile-air

126   mixture temperature is 300 K and three equivalence ratios, i.e., ϕ = 0.5, 1.0 and 2.0, of the mixture

127   are considered. To investigate the diffusion condition, a 1D counterflow diffusion volatile flame is

128   simulated also using CANTERA [42]. The mass flow rates of the biomass volatile and air inlets are

129   0.024 (kg/m^2 s) and 0.072 (kg/m^2 s), respectively, while their temperatures both are 300 K. Four

130   configurations with HCl and/or SO_2 replaced by N_2 are set up to study the effects of HCl and SO_2 on

131   potassium reaction characteristics. In total 16 cases are simulated. The grid is limited to 250 points

132   while the length of the 1D computational domain for premixed and diffusion condition is 1.0 m and

133   3.0 cm, respectively.

134

135   **3. Pulverized-biomass flame configuration and numerics**

136   A two-dimensional temporally evolving pulverized-biomass jet flame is studied (Fig. 1). The

137   computational domain has physical dimensions of 51.2 mm in both the streamwise (x) and spanwise

138   (y) directions. A uniform mesh of h = 100 μm is used, which has been demonstrated to be able to

139   resolve the flame structure [26]. Initially, high-speed primary air (10 m/s, 300 K) laden with

140   pulverized-biomass particles is set up for $|y|$ < 2.5 mm, and the 902 biomass particles follow a

141   random uniform distribution. The initial density of a particle is set to 550 kg/m^3 [43] and its

142   diameter is 25 μm, following a mono-disperse diameter distribution. The particle diameter used

143   here might be finer than common diameters of pulverized-biomass employed in other studies, e.g.,

144   60–200 μm [12, 44]. However, the particle diameter cannot be larger in order to fulfill the grid

145   resolution required by DNS and the point-particle assumption. On the other hand, this fine diameter

146   of 25 μm can be achieved with torrefied biomass [44]. Same as the 1D simulations, properties of

147   corn straw [16] are employed (Table 1). Surrounding the primary air, a hot coflow (3 m/s, 1519 K)

148   is introduced with a composition and temperature of the burnout gas of the biomass volatile at an

149   equivalence ratio of 0.45. Periodic boundary conditions are employed in all directions. Turbulent

150   fluctuations of 0.05 m/s are initially put within the shear layers between the primary air and the

151   coflow, for the purpose of facilitating the jet development. The parameters of the present

152   configuration are chosen according to our previous study on pulverized-coal flames [26]. Two-way

153   coupling between the gas and particle phases are considered and biomass particles are treated as

154   point sources.

155   Biomass pyrolysis, including K/Cl/S release, volatile-gas combustion and K/Cl/S reactions are

156   simulated. Heterogeneous reaction of solid char is not considered, since its contribution has been

157   demonstrated to be weak in small-scale pulverized-coal flames [32, 34, 45]. The char content of

158   biomass is much lower than that of coal (see Table 1). Hence, the contribution of char combustion

159   in the present pulverized-biomass flame should be even weaker and therefore can be safely ignored.
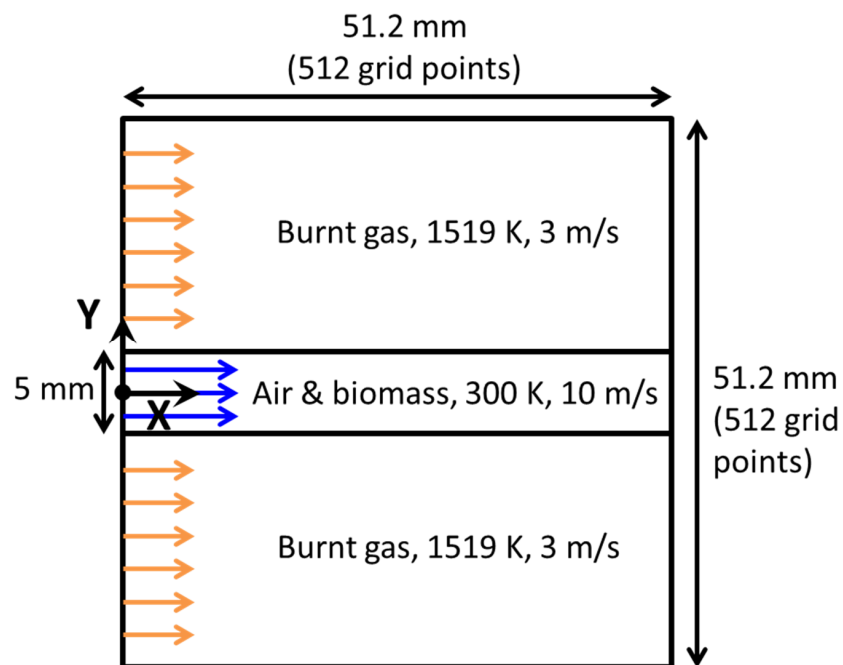
160

161   Figure 1. Schematic diagram of computational configuration. Periodic boundary conditions in all

162   directions

163   *3.1. Gas phase modeling*

164   The governing equations for the gas and biomass-particle phases are solved in the Eulerian and

165   Lagrangian frameworks, respectively, using a low-Mach-number in-house code [26, 30, 33, 34]. The

166   conservation equations for mass, momentum, species and temperature solved for the gas phase are:

167
$$D_t \rho = \dot{S}_{m,p} \tag{1}$$

168
$$D_t \left(\rho u_i \right) = -\partial_i p + \partial_j \tau_{ij} + \dot{S}_{mom,p,i} \tag{2}$$

169
$$D_t \left(\rho Y_n \right) = \partial_j \left(\rho D_n \partial_j Y_n \right) + \dot{\omega}_{Y,n} + \dot{S}_{Y,p,n} \tag{3}$$

170
$$D_t \left(\rho T \right) = \partial_j \left(\frac{\lambda}{C_{P,g}} \partial_j T \right) + \frac{\lambda}{C_{P,g}^2} \partial_j C_{P,g} \partial_j T + \dot{\omega}_T + \dot{S}_{T,p} + \dot{S}_{T,R} \tag{4}$$

171   where $D_t(\Phi) = \partial_t(\Phi) + \partial_j(\Phi u_j)$, $\partial_j \equiv \partial x_j$, ρ is gas density (kg/m^3), u_i is gas velocity (m/s), Y_n is the

172   mass fraction of the nth chemical species, T is gas temperature (K). The pressure is denoted by p, and

173   $\tau_{ij} = \mu(\partial_j u_i + \partial_i u_j - 2/3 \, \partial_k u_k \delta_{ij})$ is the viscous stress tensor. D_n is the molecular mass diffusivity

174   coefficient (m^2/s), $C_{P,g}$ and λ are the specific heat capacity (J/kg K) and thermal conductivity (W/m K)

175   of the gas mixture, respectively. $\dot{S}_{m,p}$, $\dot{S}_{mom,p,i}$, $\dot{S}_{Y,p,n}$ and $\dot{S}_{T,p}$ are the two-way coupling terms

176   considering the effects of particles on the gas. $\dot{\omega}_{Y,n}$ is the source term due to homogeneous

177   chemical reactions. In the temperature equation, the radiative heat transfer ($\dot{S}_{T,R}$), heat exchange

178   between the gas phase and biomass particles ($\dot{S}_{T,p}$), and thermal effects of homogeneous reactions

179   ($\dot{\omega}_T$) are taken into consideration. In the present study, the Lewis number (Le = 1.0) and Prandtl

180   number (Pr = 0.7) are assumed to be constant.

181

182   *3.2. Particle phase modeling*

183   The momentum equation of a Lagrangian biomass particle is:

184
$$d_t u_{p,j} = f \left(u_j - u_{p,j} \right) \big/ \tau_p \tag{5}$$

185 where $u_{p,j}$ is the particle velocity (m/s). The dynamic response time (s) of a particle is

186 $\tau_p = \rho_p d_p^2 / 18\mu$, where ρ_p is the density of the particle (kg/m^3), and d_p is its diameter (m). f is the

187 drag coefficient, which considers both the high particle Reynolds number effects and the blowing

188 effects of volatiles at the particle surface [46].

189   The particle temperature equation can be written as:

$$\mathrm{d}_t T_p = \left(Q_{conv} + Q_{rad} + Q_{dev} \right) / \left(m_p C_{P,p} \right) \tag{6}$$

191 where T_p is the temperature of the particle (K), m_p its mass (kg), $C_{P,p}$ its specific heat capacity (J/kg

192 K). The heat transfer terms by convection, radiation, and pyrolysis (devolatilization) are

193 $Q_{conv} = \mathrm{Nu}\, C_{P,g}\, m_p \left(T - T_p \right) / 3\, \mathrm{Pr}\, \tau_p$, $Q_{rad} = \varepsilon_p \pi d_p^2 \sigma \left(T_R^4 - T_p^4 \right)$,   and $Q_{dev} = -\Delta h_{dev}\, \mathrm{d}m_{vol} / \mathrm{d}t$,

194 respectively. Nu is the Nusselt number and computed by the Ranz-Marshall correlations [47]. The

195 radiation temperature (K) is calculated by $T_R = (G/4\sigma)^{1/4}$, where G is the incident radiation (W/m^2)

196 obtained via the Discrete Ordinates Method (DOM) [48]. σ is the Stefan-Boltzmann constant (5.67 ×

197 10^{-8} W/m^2 K^4). ε_p is the particle emissivity and here is set to 0.9 [39]. The

198 weighted-sum-of-the-gray-gases model (WSGGM) [49] is employed to estimate the gas absorption

199 coefficient. Finally, the mass loss rate of each biomass particle (dm_p/dt), due to the pyrolysis, is

200 predicted by the single first-order reaction model (SFOM) proposed by Badzioch and Hawskley [50].

201 The kinetic parameters of the SFOM pyrolysis model, i.e., A_v (2.5 × 10^9 s^{-1}), E_v (11 × 10^4 J/mol) and

202 Q_v (1.10), have been calibrated by the bio-CPD model [38], as in [30, 33, 34].

203

204 *3.3. Gas phase chemistry*

205   Same as in Section 2, the oxidization of hydrocarbon biomass volatile and the reactions of

206 potassium species are modeled by the DRM22 skeletal mechanism [37] and the detailed alkali

207 reaction mechanism [21], respectively. The compositions of the volatile gas can be found in Table 2,

208 including the non-hydrocarbon compounds of potassium, sulfur and chloride.

209   The release rate of potassium from biomass particles is assumed to be proportional to the

210 volatile release rate [26, 34], since the potassium vapor generated inside the porous structure of a

211 biomass particle will be transported outward by the volatile yielded during the pyrolysis stage.

212 Besides, in our previous study the alkali release from a coal particle was found proportional to its

213 burnout during the early combustion stage [18]. Similarly, the release rates of sulfur and chlorine are

214 also assumed to be proportional to the volatile release rate here.

215

216 *3.4. Numerical schemes*

217   The numeric of our in-house code is based on an approach previously validated for both DNS

218 and LES [51, 52]. A second-order Crank-Nicolson scheme is employed for the time advancement. A

219 second-order central difference scheme is applied to all terms in the momentum equation and the

220 scalar diffusion terms in the species and temperature equations. In order to secure the scalar

221 boundedness, a Quadratic Upstream Interpolation for Convective Kinematics (QUICK) scheme is

222 used for the scalar advection terms in the species and temperature equations. An Alternating

223 Direction Implicit (ADI) approach has been adopted, and semi-implicit tridiagonal/pentadiagonal

224 equations are solved separately for each direction. A second-order Runge-Kutta (RK2) scheme is

225 employed to explicitly advance the particle equations.

226

4. Results and discussion

### 4.1. Transformation characteristics of potassium species in 1D premixed flame

The reactions of potassium species in 1D premixed volatile flames have been investigated for three equivalence ratios (ϕ = 0.5, 1.0 and 2.0), representing fuel-lean, stoichiometric and fuel-rich conditions. From Fig. 2, it can be found that the concentration of KOH rapidly decreases in the initial unburned region with T = 300 K, which should be attributed to the following two reaction paths:

$$2KOH \rightarrow K_2O_2H_2 \text{ (R1)};$$

$$KOH + HCl \rightarrow KCl + H_2O \text{ (R2)}, \quad 2KCl \rightarrow K_2Cl_2 \text{ (R3)}.$$
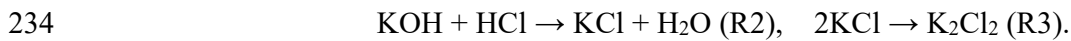
First, KOH is consumed to generate $K_2O_2H_2$ via Reaction R1. In addition, KOH also reacts with HCl in the volatile as Reaction R2, and K_2Cl_2 is subsequently formed through Reaction R3. $K_2O_2H_2$ and K_2Cl_2 are the two major potassium species in the initial unburned region. It should be noted that at low temperature, the potassium is in condensed form, possibly as aerosol. Hence, the results in the initial unburned region of the canonical laminar flame are questionable. However, this issue will get relieved in the following investigation of 2D pulverized-biomass flame (Section 4.3) because the potassium is released along with volatile and therefore at much higher temperature. When the combustion happens and therefore the temperature increases around Distance of 0.15 cm, $K_2O_2H_2$ and K_2Cl_2 are then decomposed to KOH and KCl, respectively, and further transform to other potassium species, e.g., K, KO_2, KSO_2, $KHSO_4$ and K_2SO_4. In the post-flame region, the potassium species then gradually evolve towards equilibrium. It can be observed that KOH is the most significant potassium product (~10^3 ppm) for all the three equivalence ratios, while KCl has the second highest concentration (~10^2 ppm). The sulfurous potassium species K_2SO_4 is found to be the third major potassium product (34 ppm) under the fuel-lean condition; while under the stoichiometric

12

and fuel-rich conditions, the third major potassium product changes to atomic potassium K (> 60 ppm). Another minor potassium species, KSO$_3$Cl, has a maximum concentration less than 0.01 ppm during the whole reaction process for all the three equivalence ratios and therefore is not shown in the figure.
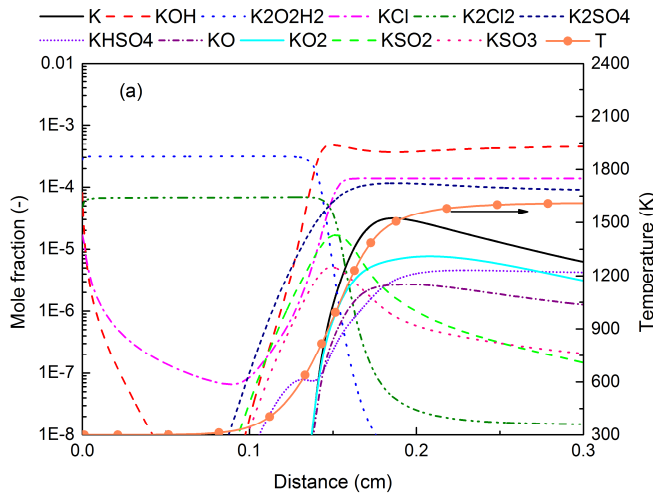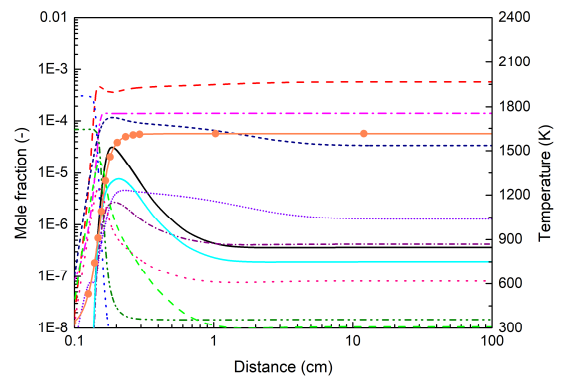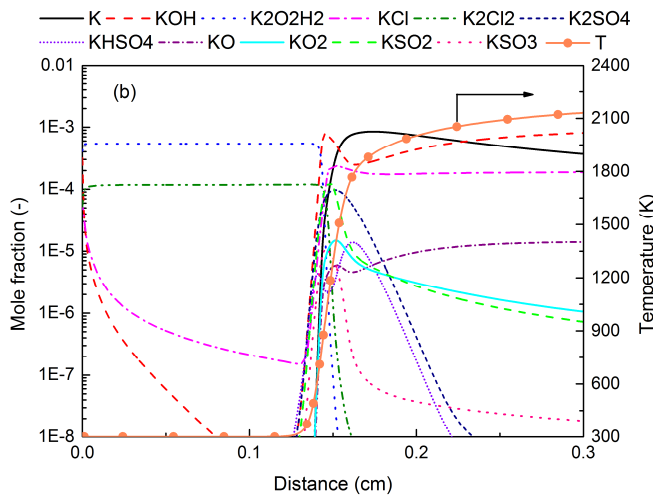
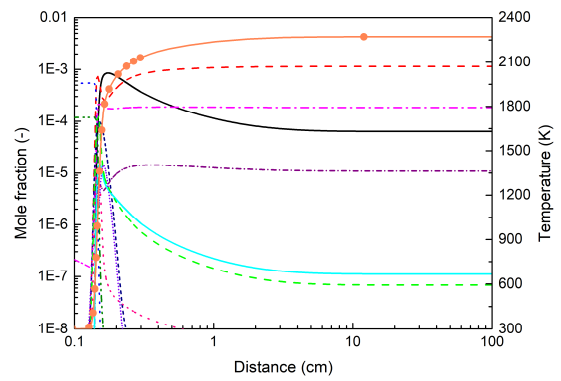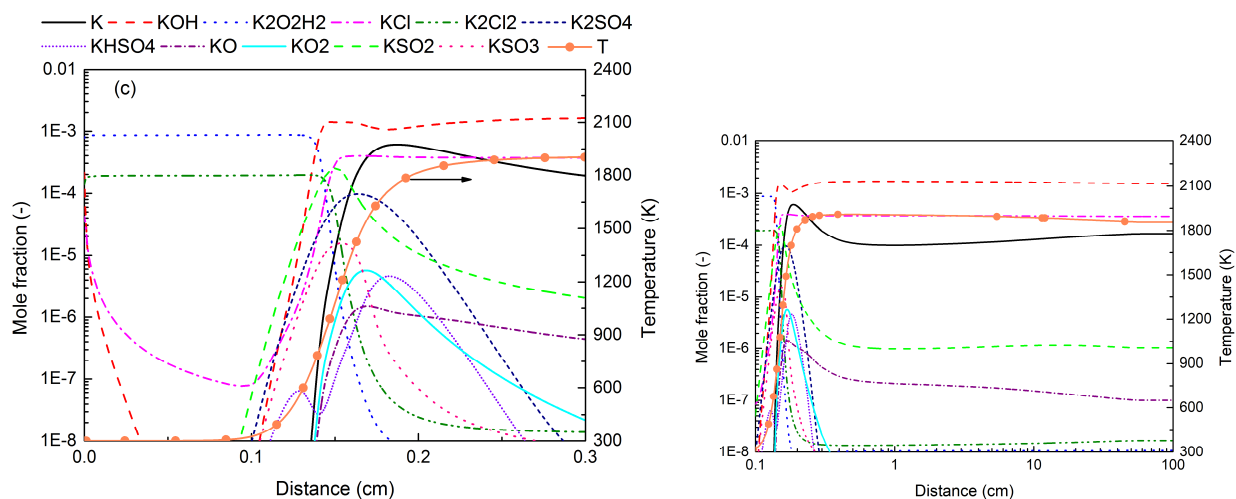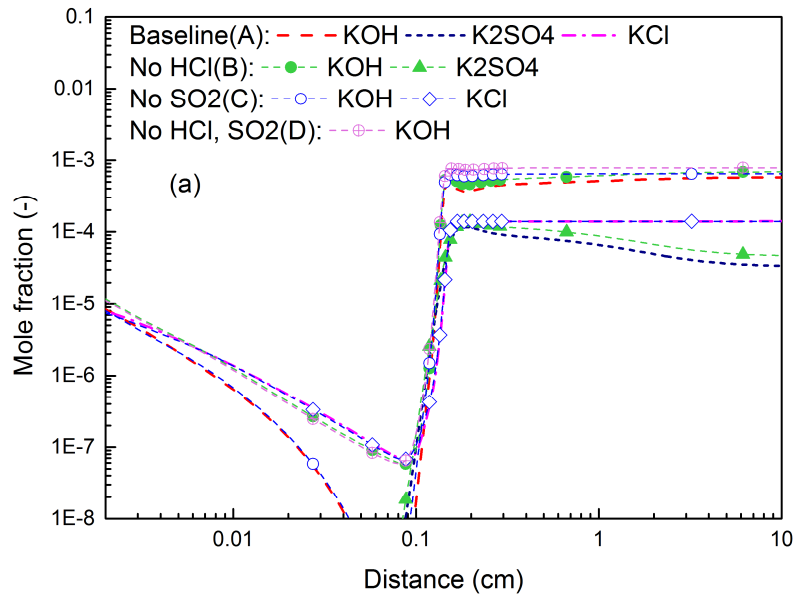Figure 2. Potassium species distribution versus distance along the 1D premixed volatile flame at equivalence ratio $\phi = 0.5$ (a), $\phi = 1.0$ (b) and $\phi = 2.0$ (c). The heat release zone is zoomed in and shown on the left side while the overall flame is shown on the right side.

To study the effects of HCl and SO_2 on potassium transformation characteristics, three additional configurations have been employed, which are Case B (HCl in the volatile is replaced by N_2), Case C (SO_2 in the volatile is replaced by N_2) and Case D (both HCl and SO_2 in the volatile are replaced by N_2). The original case is referred to as baseline Case A. Three simulations ($\phi = 0.5$, 1.0 and 2.0) are performed for each Case A/B/C/D. The comparison of the representative potassium species KOH, KCl and K_2SO_4 is shown in Fig. 3. The profiles are plotted until Distance of 10 cm, as it can be found in Fig. 2 that the potassium reactions almost reach equilibrium at this position. KOH is found to be the main potassium product for the four cases. When HCl and/or SO_2 is presented, a minor part of potassium is transformed to KCl and/or K_2SO_4. However, the mole fraction of the produced KCl and/or K_2SO_4 is much lower than that of KOH. Hence, the profiles of KOH are close to each other for the four cases in the combustion and post-flame regions.
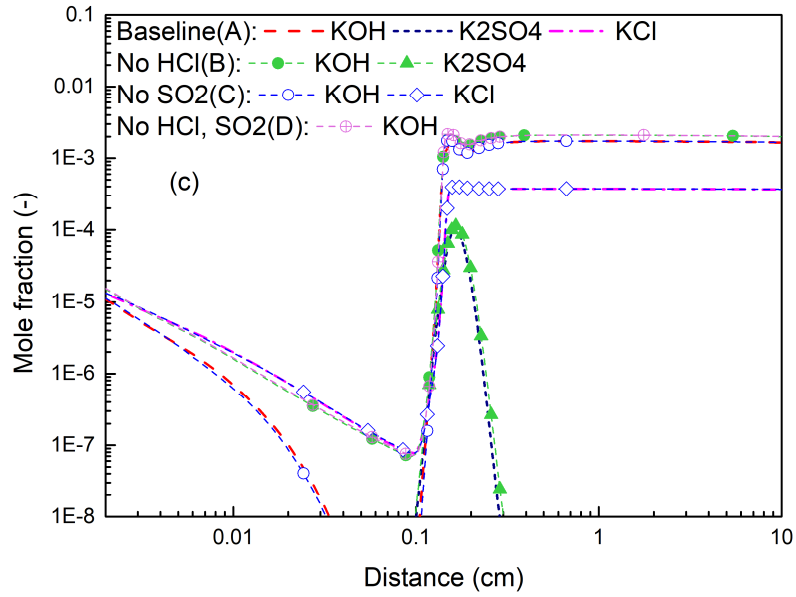
(a)

274

275

(b)

276

277
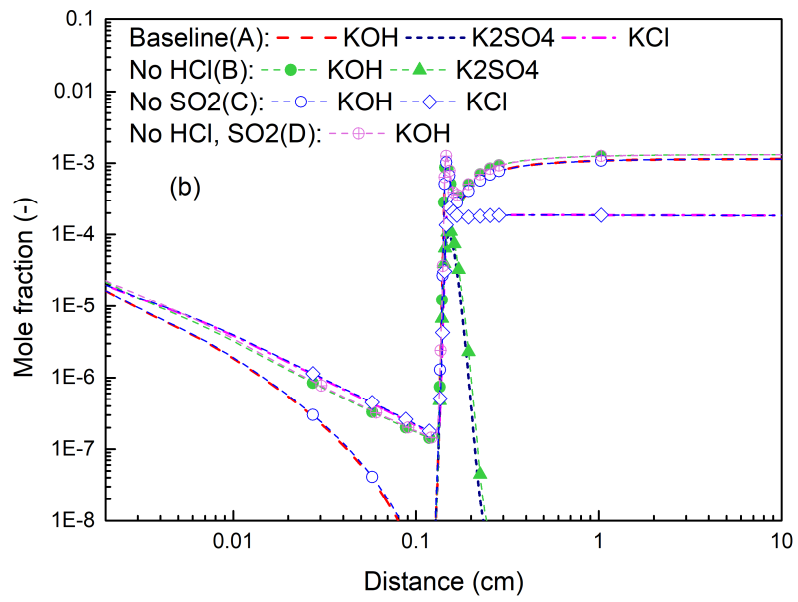
Figure 3. Comparison of potassium species distribution versus distance along the 1D premixed volatile flame between Case A (the baseline case), Case B (HCl replaced by N_2), Case C (SO_2 replaced by N_2) and Case D (both HCl and SO_2 replaced by N_2) at equivalence ratio $\phi = 0.5$ (a), $\phi = 1.0$ (b) and $\phi = 2.0$ (c).

4.2. Transformation characteristics of potassium species in 1D diffusion flame

To further investigate the response of potassium species in diffusion flame, other four cases have been set up: Case E (the baseline case), Case F (HCl in the volatile is replaced by N_2), Case G (SO_2 in the volatile is replaced by N_2) and Case H (both HCl and SO_2 in the volatile are replaced by N_2). Comparison among these cases on the representative potassium species K, KOH, KCl and K_2SO_4 is shown in Fig. 4. It may be noted that only the region of the mixture fraction $Z < 0.6$ are shown, because a higher mixture fraction is hardly observed in the following 2D DNS study (see Fig. 7 below). The mixture fraction could be calculated as $Z = 1.0 - Y_{N2}/0.767$. For the present two-stream mixing case of 1D diffusion flame, $Z = 0$ and $Z = 1$ indicate the oxidizer and biomass-volatile streams, respectively. The positions of $\phi = 0.5$, 1.0 and 2.0 in the mixture fraction space are also illustrated in Fig. 4. It can be found that in the fuel-lean region the mole fraction of K increases rapidly with Z for all the cases. In the very rich region of $Z > 0.5$, the profile of K drops in

295 the cases (E/F) with SO_2, which is not observed in the cases (G/H) without SO_2. Both KOH and KCl

296 show a monotonically increasing trend along with Z, although the increasing rate get suppressed at

297 the stoichiometric condition. For Na_2SO_4, it reaches a concentration of ~20 ppm at the fuel-lean

298 region around $Z = 0.05$, but becomes minor (< 0.1 ppm) for all the other conditions. Similar as in the

299 previous premixed flames, the profiles of KOH in the four cases here are also close to each other,

300 because the productions of sulfurous and chloric potassium species are limited.

301
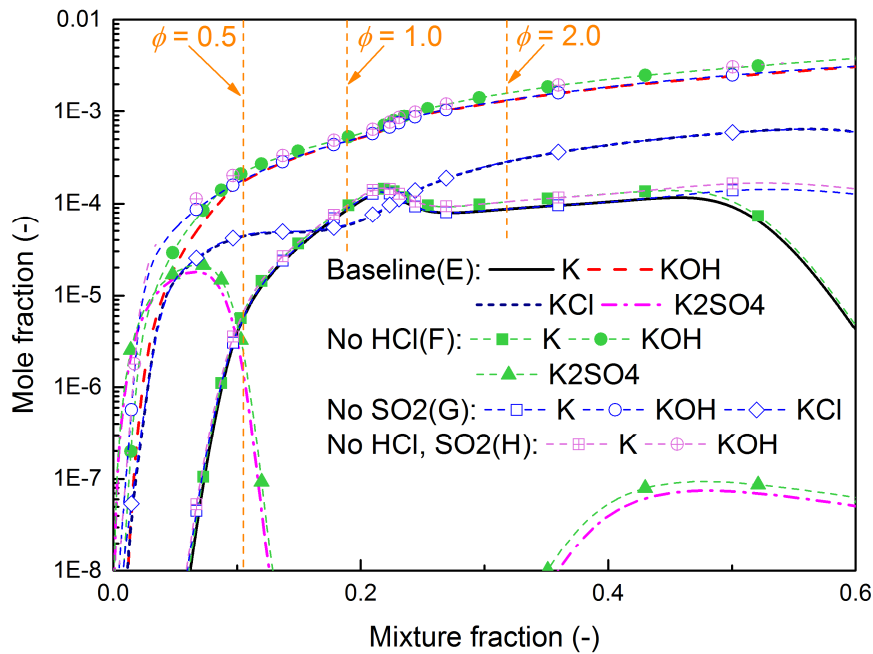
303 Figure 4. Comparison of potassium species distribution in the mixture fraction space of the 1D

304 diffusion volatile flame among Case E (the baseline case), Case F (HCl replaced by N_2), Case G

305 (SO_2 replaced by N_2) and Case H (both HCl and SO_2 replaced by N_2).

306 *4.3. Characteristics of the 2D pulverized-biomass flame*

307   The transformation of potassium species in the 2D pulverized-biomass flame is then

308 sequentially examined. Figure 5 shows the evolution of some important quantities of the flame: (a)

309 gas temperature and particle burnout, (b) OH mass fraction, (c) K mass fraction, (d) KOH mass

310 fraction, and (e) flame index and particle temperature. In the early stage of $t = 10–15$ s, biomass

311 particles in the jet shear layers are heated by the high-temperature coflow. Volatiles including

312 potassium, chlorine and sulfur compounds are then released from these particles via the pyrolysis

313 process. Isolated flame structures [27, 34] can be observed at $t = 15$ ms, which are formed due to

314 individual particles ignited in the shear layers. At $t = 20$ ms, more and more particles get ignited and

315 Y_{OH} propagates, representing a strong heat release of the rapid spreading flame. Atomic potassium K

316 has a high concentration in the high-temperature burning zone, while KOH accumulates around the

317 ignited particles. Finally, at $t = 30$ ms, the flame tends to be weak as most of the biomass particles in

318 the computational domain burn out. However, a wider flame regime can be observed since the

319 turbulent mixing continues. The concentrations of OH radical and atomic K drop, but that of KOH

320 remains a significant level.
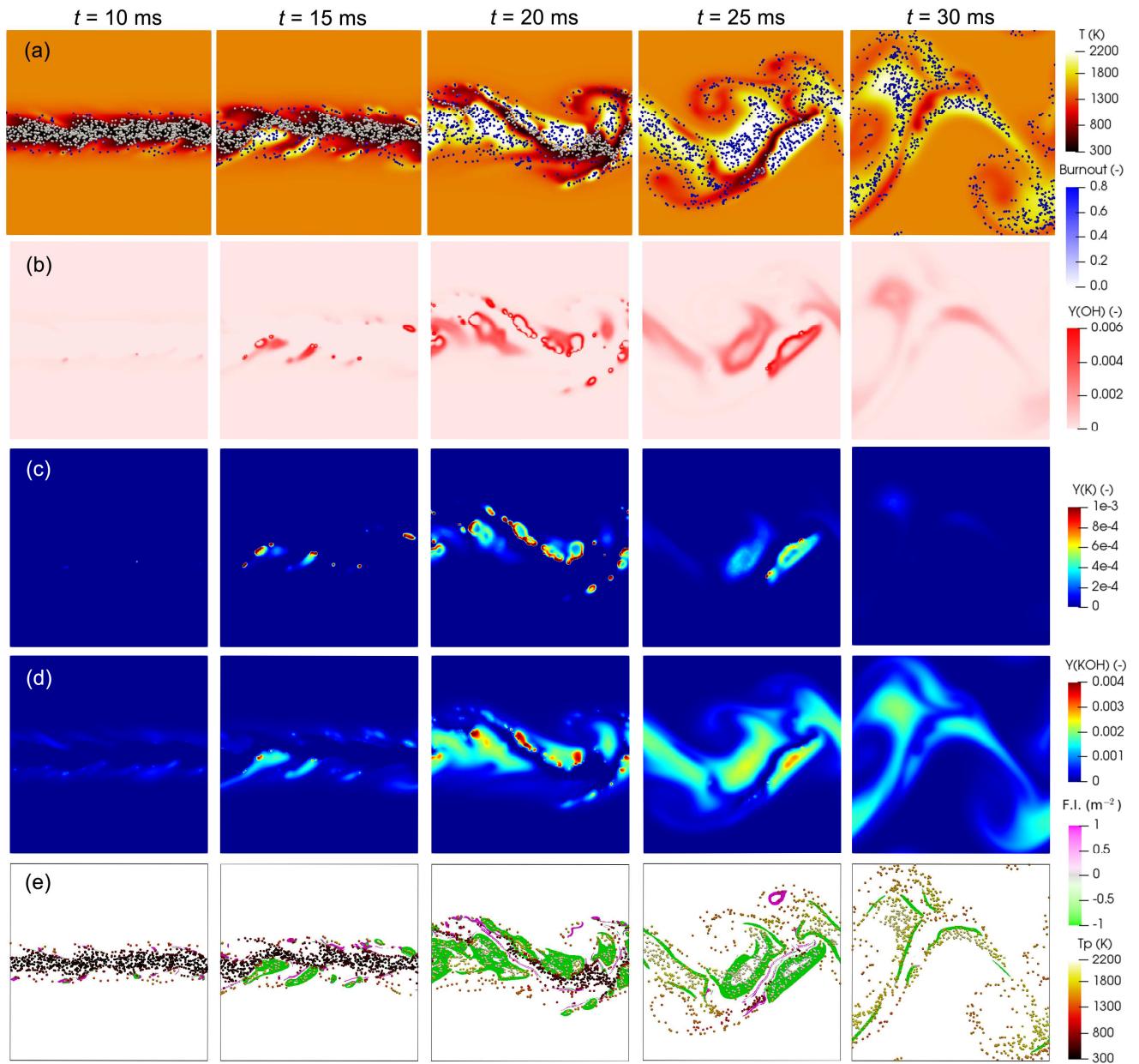
Figure 5. Time evolutions of instantaneous distributions of the (a) gas temperature and particle burnout, (b) OH mass fraction, (c) K mass fraction, (d) KOH mass fraction and (e) flame index and particle temperature.

Based on the spatial gradients of the mass fractions of volatile fuel and oxidizer, the flame index, F.I. [24, 53, 54], can be computed as: F.I. $= \nabla Y_f \cdot \nabla Y_{O2}$, where $Y_f = Y_{CH4} + Y_{CO} + Y_{C2H2} + Y_{H2}$. Positive F.I. values indicate premixed flame regimes, while negative ones for diffusion flame. F.I. distribution of the biomass flame is shown in Fig. 5e for the regions where the heat release rate exceeds 10^7 W/m^3 and therefore are actively reacting regions. The maximum heat release rate in the 2D domain

330   is 3.03×10^{10} W/m^3. It can be found that at the beginning stage of $t < 15$ ms, the first ignition of

331   biomass particles is controlled by premixed combustion. Then after the biomass jet reaches actively

332   reacting state, the volatile released from particles accumulates before burning and therefore leads to a

333   dominant diffusion combustion mode [26].

334   Figure 6 shows the instantaneous distributions of all the twelve potassium species considered in

335   the DNS at $t = 20$ ms. The isoline of $\phi = 1$ is superimposed, which represents the stoichiometric

336   condition of combustion between the biomass volatile and the oxidizer. It can be found that atomic K

337   has a high concentration in the regime close to the isoline, where the volatile fuel is actively burning

338   and the temperature is high. Both KOH and KCl feature a high concentration in the fuel-rich region

339   (inside the isoline), and a moderate concentration in the fuel-lean region (outside the isoline). KOH

340   is the released potassium species along with the volatile, while the high concentration of KCl in the

341   fuel-rich region can be explained by the Reaction R2. $KHSO_4$ and K_2SO_4 are the two major sulfated

342   potassium species, which mainly form in the fuel-lean region, but their concentrations are much

343   lower than the potassium chloride KCl. The two favored potassium species in the pre-combustion

344   mixture K_2Cl_2 and $K_2O_2H_2$ are observed only in the fuel-lean region, since they will decompose

345   under high temperature. The other five minor potassium species, i.e., KO, KO_2, KSO_2, KSO_3 and

346   KSO_3Cl, are produced under the fuel-lean condition, while KSO_2 achieves a high concentration in

347   the fuel-rich region where abundant potassium and sulfur exist.
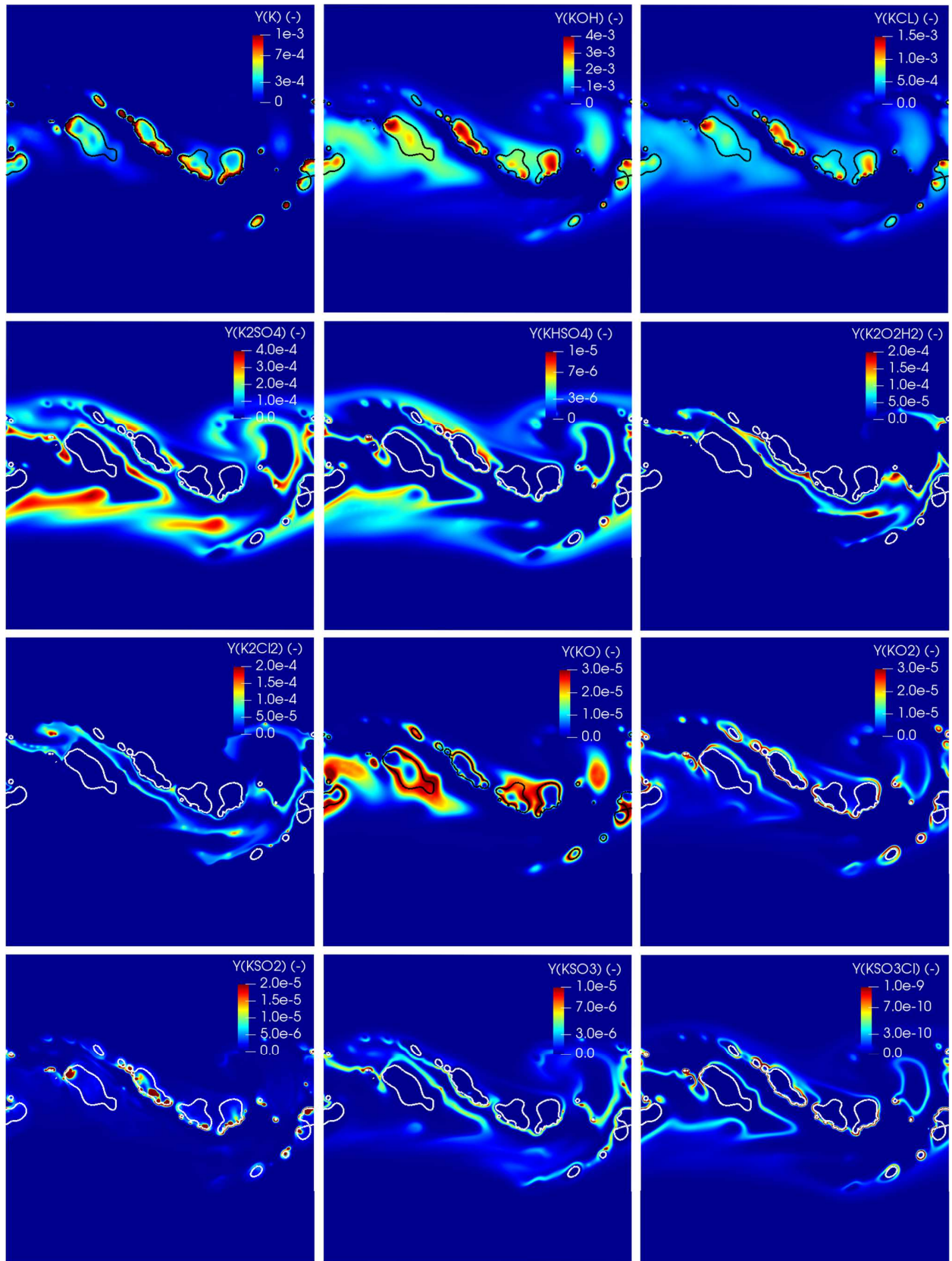
348

349   Figure 6. Instantaneous distributions of all the twelve potassium species at t = 20 ms. The isoline of ϕ

350   = 1 is superimposed.

351

4.4. Potassium species dynamics

Figure 7 shows the instantaneous scatter plots of six representative potassium species against the mixture fraction at t = 20 ms. For the three-stream mixing in the 2D pulverized-biomass flame, the mixture fractions of the volatile released from biomass particles (the fuel stream), the air jet carrying these particles (the oxidizer stream) and the high-temperature coflow are Z = 1, Z = 0 and Z = 0.093, respectively. K, KCl and KOH are the three major potassium species in the reaction products. The distributions of Y_{KCl} and Y_{KOH} are almost linear with Z, while that of Y_K is subtler. Y_K stays almost zero for the lower range of Z < 0.05, to then increases rapidly until Z = 0.22, and then holds a moderate increasing rate for the fuel-rich regime of Z > 0.22. Finally, Y_{KHSO4}, Y_{K2SO4} and Y_{K2O2H2} feature a single-peak distribution within the fuel-lean regime of $Z < Z_{st}$ = 0.189.

The potassium profiles obtained from 1D diffusion flames are also shown in Fig. 7 with the blue solid line and the red dash line corresponding to the lowest and highest strain rates, respectively. It can be found that the high-strain rate (red dash line) helps to enhance the transformation of KOH to K, KHSO$_4$ and K$_2$SO$_4$, while the production of KCl is insensitive to the strain rate. This is because the KCl-formation reactions are almost instantaneous (of the order of a few micro seconds), and therefore can hardly be affected by the relatively much slowly varying strain rate. It can also be observed in Fig. 2 that the reaction zone of KCl is much thinner than the other potassium products. Compared with the line plots from 1D diffusion flames, the DNS scatters generally follow a similar trend, but lots of data points fall outside the region between the red dash and blue solid lines. These points are likely to represent the unsteadiness and/or partial premixing of the reactants, because the volatile ejected from the particles is rapidly mixed with the ambient air in a partially premixed mode, as in [55]. Besides, the radiation heat loss also contributes to the discrepancy between line plots from

1D diffusion flames and DNS scatters.
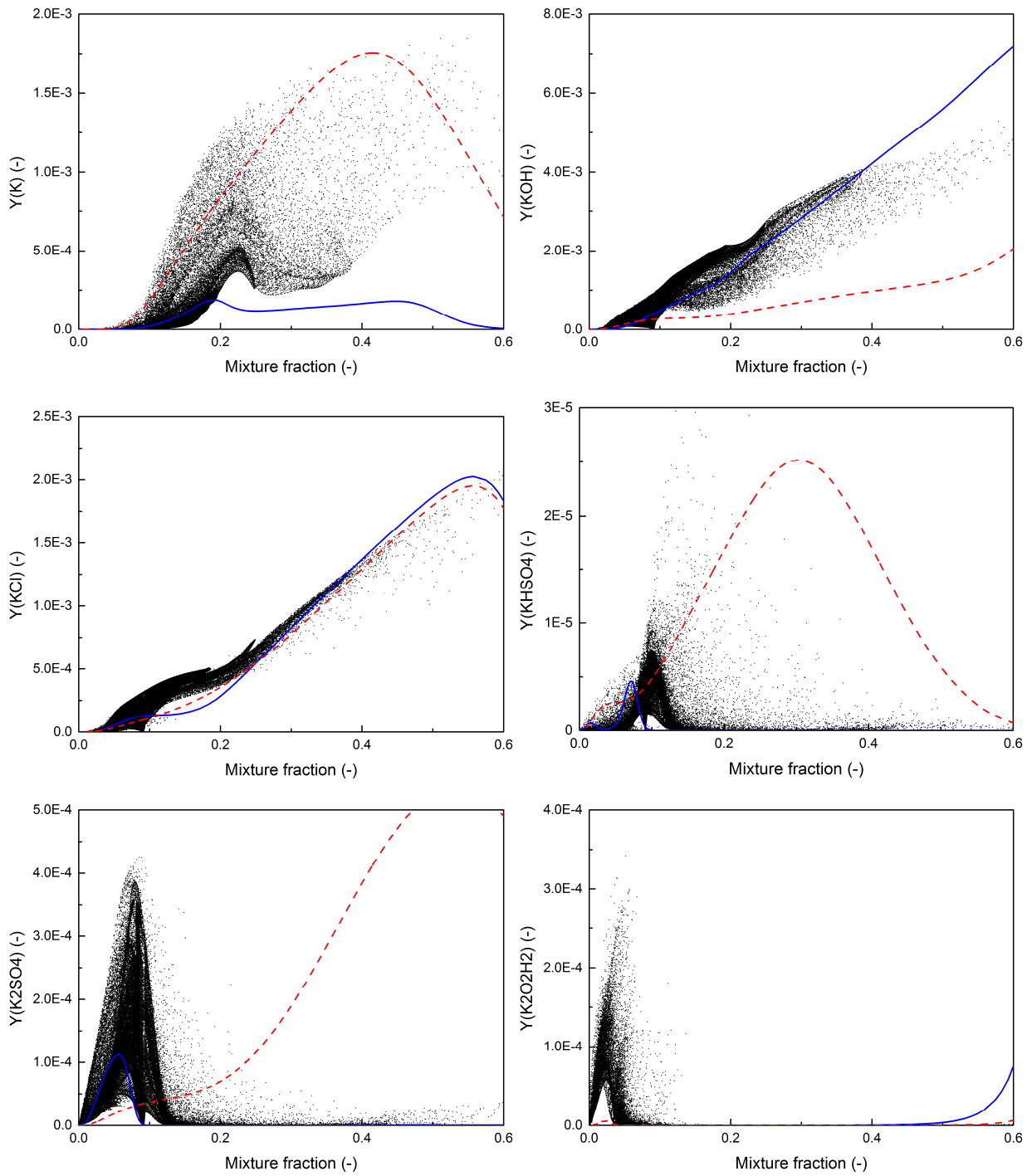
378 Figure 7. Scatter plots of instantaneous mass fractions of K, KCl, KOH, KHSO$_4$, K$_2$SO$_4$ and K$_2$O$_2$H$_2$

379 against Z at t = 20 ms. Blue solid line and red dash line are the potassium profiles obtained from 1D

380 counterflow diffusion flames, corresponding to the lowest (21 s^{-1}) and highest strain rates (8556 s^{-1}).

381

382   *4.5. Statistics of the 2D pulverized-biomass flame*

383   Figures 8 and 9 show the time evolutions of the mean mass fractions of OH, HCl, SO$_2$, Z_{vol} and

384   six representative potassium species, and the mean gas temperature of the biomass flame. All of

385   these quantities are averaged over the entire 2D computational domain. Z_{vol} is the volatile mixture

386   fraction, which can be obtained from:

387    $$\mathrm{D}_t\left(\rho Z_{vol}\right) = \partial_j\left(\rho D_Z \partial_j Z_{vol}\right) + \dot{S}_{Y,p,vol} \tag{7}$$

388   where D_Z is the diffusivity coefficient of volatile gas (m^2/s) and its value is set equal to the thermal

389   diffusivity. $\dot{S}_{Y,p,vol}$ is the source term of the volatile mass released from biomass particles.
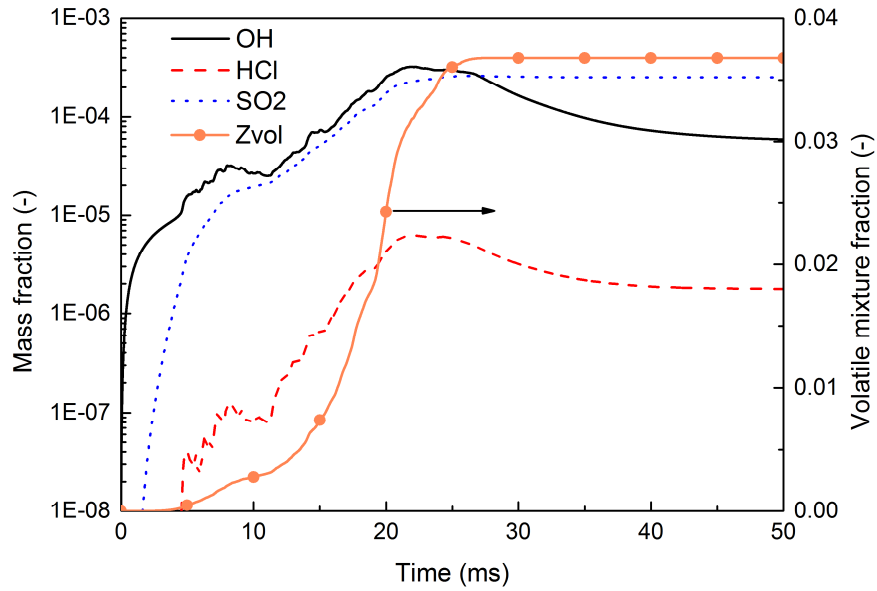

390

391   Figure 8. Time evolutions of the mean mass fractions of OH, HCl, SO$_2$ and Z_{vol} averaged over the 2D

392   computational domain.

393   It can be observed that the first ignition of the biomass jet happens at t = 5 ms. The mass

394   fractions of potassium species and the gas temperature start to increase and small peaks can be found

395   for Y_{OH} and Y_{HCl}. This is because the volatile fuel gets ignited around some particles, which in turn

396   heats up the particles rapidly and therefore bring a high flux of volatile release. After t = 15 ms, the

397   biomass jet is actively burning which reflects in both T and Z_{vol} increase rapidly, same as the mass

398   fractions of Y_{OH}, Y_{HCl}, Y_{SO2}, Y_{KOH} and Y_{KCl}. After $t = 30$ ms, both T and Z_{vol} remain almost constant,

399   indicating the end of the combustion of the biomass jet. However, although the average of gas

400   temperature in the domain becomes stable, its variance is further decreasing due to turbulent mixing

401   of the hot burnout gases and the surroundings. This explains the variation of the species mass

402   fractions after $t = 30$ ms, e.g. the decreasing of Y_{HCl} due to Reaction R2. At the end of the simulation

403   ($t = 50$ ms), KOH is found to be the major potassium product. Comparing the DNS predictions at the

404   end of the simulation to a reference equilibrium calculation by CANTERA [42] of a

405   zero-dimensional (0D) homogeneous reactor under the temperature of 1538 K, which is the final

406   averaged temperature of the 2D DNS domain, the relative errors are of 2.07% for KOH, 2.93% for

407   KCl and 21.85% for K_2SO_4. The larger error for K_2SO_4 should be attributed to the slower sulfation

408   reactions, as shown in Fig. 2a, and therefore it would take a much longer time for K_2SO_4 to reach

409   equilibrium. Furthermore the 2D DNS domain does not reach a homogeneous state at $t = 50$ ms,

410   which also contributes to the discrepancy between the DNS predictions and equilibrium results.

411
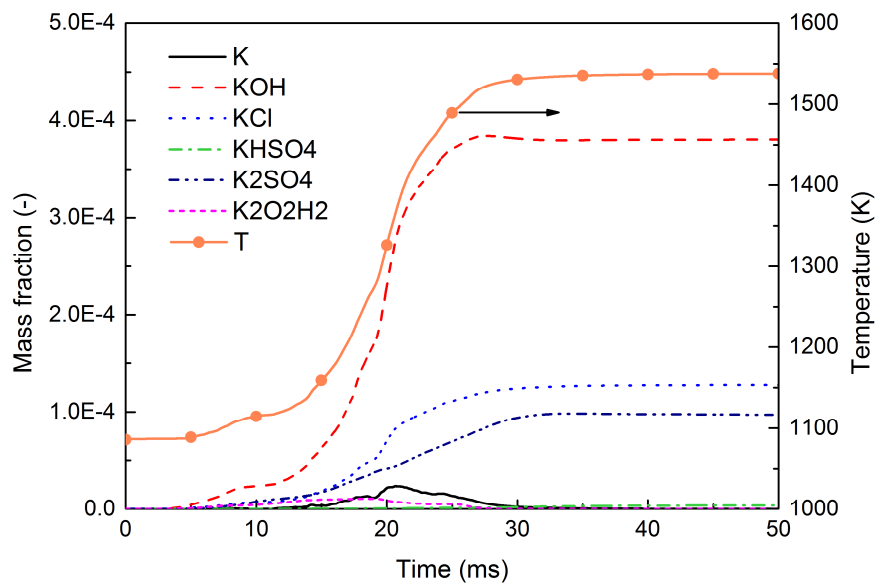
412

413   Figure 9. Time evolutions of the mean mass fractions of K, KOH, KCl, KHSO$_4$, K$_2$SO$_4$ and K$_2$Cl$_2$,

414   and the mean gas temperature.

The major pathways of potassium transformation in the pulverized-biomass flame is summarized in Fig. 10. It can be found that HCl reacts with potassium species in a straightforward way, i.e., $HCl + KOH \rightarrow KCl + H_2O$ and $HCl + K \rightarrow KCl + H$. In contrast, the formation of sulfated potassium species is more complex. The SO_2 is first oxidized to SO_3, to then reacts with KOH to form $KHSO_4$, and finally produce K_2SO_4 through a shuffle reaction, $KHSO_4 + KOH \rightarrow K_2SO_4 + H_2O$.
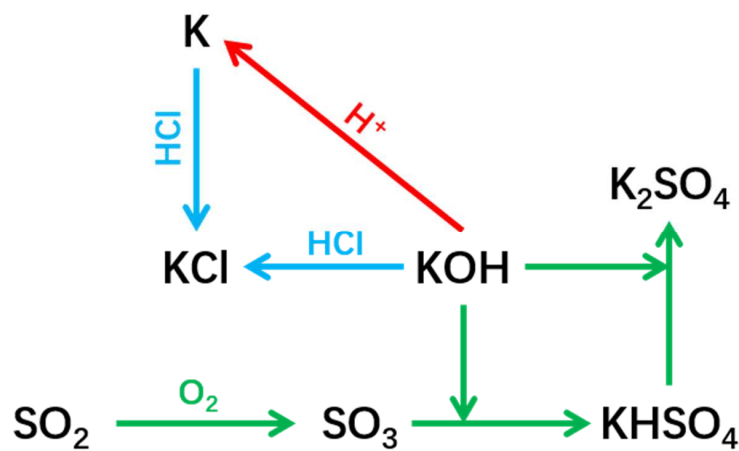
Figure 10. Major pathways of potassium transformation during pulverized-biomass combustion.

4.6. Effects of HCl and SO₂ on potassium emissions in the 2D pulverized-biomass flame

Three additional DNS cases are set up to investigate the effects of HCl and SO_2 on potassium transformation characteristics: Case K (HCl in the volatile is replaced by N_2), Case L (SO_2 in the volatile is replaced by N_2) and Case M (both HCl and SO_2 in the volatile are replaced by N_2). Case J refers to the original baseline DNS case. The comparison between the four cases is shown in Figure 11. In all the cases, KOH is the main potassium product at the end of the simulation. However, with HCl and/or SO_2 present, part of KOH is transformed to KCl and/or K_2SO_4, respectively. Based on the initial mass fractions (Y_0) of KOH/HCl/SO_2 in the volatile (Table 2) and the final mass fractions (Y_{final}) of KCl/K_2SO_4 in the burnout gases, we can calculate the conversion rate (α) of KCl and

432   K_2SO_4 as:

$$\alpha_{KCl} = \frac{Y_{\text{final,KCl}}/M_{KCl}}{Z_{vol,\text{final}} \cdot \min\left(Y_{0,KOH}/M_{KOH}, Y_{0,HCl}/M_{HCl}\right)} \times 100\% \tag{8}$$

$$\alpha_{K_2SO_4} = \frac{Y_{\text{final},K_2SO_4}/M_{K_2SO_4}}{Z_{vol,\text{final}} \cdot \min\left(0.5 Y_{0,KOH}/M_{KOH}, Y_{0,SO_2}/M_{SO_2}\right)} \times 100\% \tag{9}$$

435   where M denotes the molar mass. The obtained conversion rate of KCl in Case L is $\alpha_{KCL} = 95.1\%$,

436   while that of K_2SO_4 in Case K is $\alpha_{K2SO4} = 14.7\%$. The conversion rate of KCl is much higher than

437   that of K_2SO_4, indicating HCl has a much stronger ability to react with potassium species than SO_2.

438
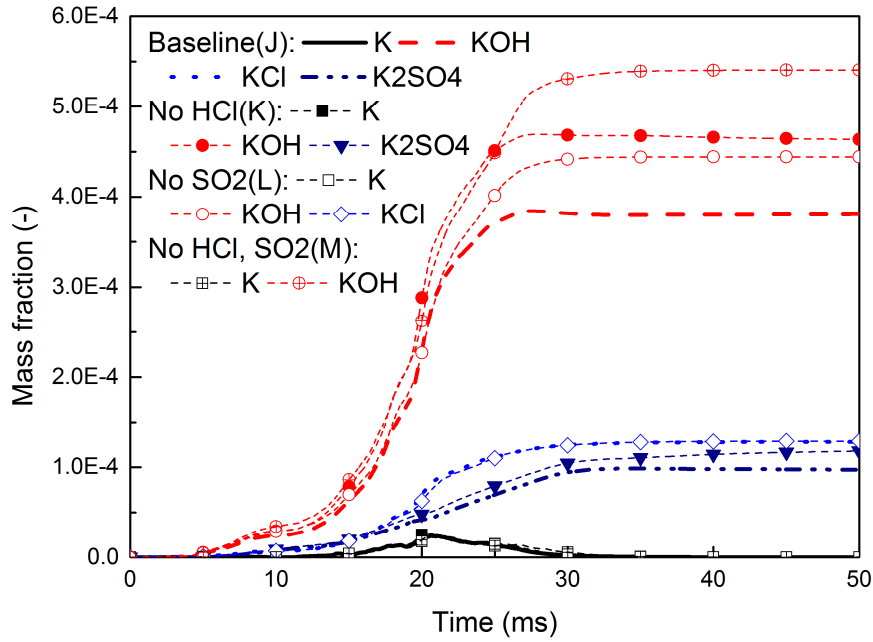
440   Figure 11. Comparison of time evolutions of the mean mass fractions of potassium species among

441   Case J (the baseline case), Case K (HCl replaced by N_2), Case L (SO_2 replaced by N_2) and Case M

442   (both HCl and SO_2 replaced by N_2).

443   *4.7. Comparison of potassium emission characteristics in 1D and 2D flames*

444   The 1D premixed flame simulations (Fig. 2) show that KOH is the most significant potassium

445   product under various equivalence ratios in fuel-lean, stoichiometric and fuel-rich conditions. This is

446   consistent with the 1D diffusion flame simulation results (Fig. 4). However, some discrepancies can

447 be observed between the premixed and diffusion flame predictions. For instance, the premixed flame

448 results show that the second major potassium product is KCl under all the conditions, which is not

449 the case in the diffusion flame under stoichiometric condition, where atomic K has a higher

450 concentration than KCl. The reason of the discrepancy should be that the 1D diffusion flame is

451 strained while the 1D premixed flame is freely propagating. In fact, Fig. 7 indeed shows that a higher

452 strain rate could promote the production of K, while KCl is insensitive to the variation of strain rate.

453 Finally, the statistics of the 2D biomass flame also demonstrates that KOH is the major potassium

454 product. The overall equivalence ratio of the 2D flame is 0.55 (corresponding to a mixture fraction Z

455 = 0.094), and therefore its potassium emission statistics are close to that of the 1D flames under the

456 fuel-lean condition.

457

458 **5. Conclusions**

459   The emission characteristics of potassium species in biomass combustion are numerically

460 investigated via 1D premixed/diffusion flames of biomass volatile, and a 2D pulverized-biomass

461 flame. Complex chemistry has been used for both the volatile hydrocarbon combustion and the

462 potassium species reactions. From the 1D premixed flame simulations, it is found that KOH is the

463 most significant potassium product for all the three equivalence ratios, while KCl has the second

464 highest concentration. The 1D diffusion flame simulations also support that KOH is the major

465 potassium products while the productions of sulfurous and chloric potassium species are secondary.

466   The emission characteristics of the potassium species in a 2D pulverized-biomass flame are then

467 examined. The instantaneous distribution characteristics show that KOH, KCl and K are the three

468 major potassium species in the reaction zone. The distributions of Y_{KCl} and Y_{KOH} are almost linear